Materials Advances

ROYAL SOCIETY OF CHEMISTRY

PAPER

View Article Online
View Journal | View Issue

Cite this: *Mater. Adv.*, 2026, 7, 2971

Exploring the storage applications of FeS–ZnO nanocomposite as a negative electrode for asymmetric supercapacitors

Junaid Riaz [a] and Amina Bibi*[b]

Received 28th September 2025,
Accepted 30th January 2026

DOI: 10.1039/d5ma01110h

rsc.li/materials-advances

This paper reports a low-cost and facile wet-chemical method to fabricate FeS–ZnO nanocomposites, offering promising potential for next-generation supercapacitor applications. The FeS–ZnO electrode exhibits rapid faradaic redox reactions and sufficient electrochemical double-layer charge storage in an aqueous medium, achieving a high specific capacitance of 485.10 F g^{-1} within a potential range of −0.8 to 0.0 V. The FeS–ZnO composite outperforms its components, FeS and ZnO, by exhibiting enhanced electrochemical properties. An asymmetric supercapacitor utilizing a FeS–ZnO‖MnO_2 configuration in KOH electrolyte demonstrates exceptional rate capability, delivering a capacitance of 145.62 F g^{-1}, an extended voltage window of 1.6 V, and reliable performance over 10 000 cycles. The FeS–ZnO nanocomposite shows great promise as an efficient electrode material for next-generation energy storage, delivering a high energy density of 51.77 Wh kg^{-1} along with a power density of 4000 W kg^{-1}.

1. Introduction

Currently, we face pressing challenges of energy deficits and ecological degradation. In light of these issues, there is a growing need for more efficient and sustainable energy sources, as well as the development of advanced energy storage systems.[1] Electrical energy is the primary sustainable energy source for consumer electronics, medical equipment, hybrid electric vehicles, and other comparable technologies.[2] The development and enhancement of supercapacitors (SCs) arose from a pressing demand for electrical energy storage solutions characterized by high power density, extended cyclic lifespan, optimal capacity retention, and ecological sustainability. The increasing consumption of electrical energy in contemporary civilization fuels this demand. The need for portable energy storage devices is expected to be fulfilled by SCs due to their high-power density (1–10 kW kg^{-1}), rapid charge–discharge speeds, and long-life cycle (>100 000 cycles).[3] In recent years, extensive research has been conducted on the energy and power densities of SCs, as enhancing these attributes is crucial for improving the performance and efficiency of various applications. The symmetrical cell design, independently optimized capacitance, and extended voltage windows (up to 2.2 V) for both the positive and negative electrodes in asymmetric supercapacitors (ASCs) contribute to enhanced energy density.[4] Recently, the development of advanced electrode materials has been considered a key strategy to enhance the performance of next-generation energy storage devices, including asymmetric supercapacitors.[5]

The two most widely recognized types of supercapacitors are electric double-layer capacitors (EDLCs) and pseudocapacitors. At the electrode/electrolyte interface, they quickly undergo faradaic redox reactions between the active and electrolyte components to store energy. On the other hand, EDLCs are made of carbon-based materials and use an efficient ion adsorption/desorption process to store energy. Recent years have seen significant progress in both types of SCs, with extensive research conducted on both theoretical and experimental aspects.[6–8] Recent studies on nickel cobalt hydroxide-based hollow structures have demonstrated that rational structural engineering, such as ion exchange–etching strategies, can significantly enhance electrochemical activity, charge transfer, and energy density in hybrid supercapacitors. However, SCs' limited applicability across several sectors is due to their considerably lower energy densities and overall performance.[9–12] The electrochemical performance of SC is primarily influenced by the electrode material, which encompasses a diverse array of transition metal oxides. RuO_2, an active electrode material, is distinguished by its elevated specific capacitance.[13] However, its widespread use as an electrode material in SCs has been limited by its toxicity as well as its cost.[14,15] As a result, considerable effort has been devoted to SCs to achieve high specific capacitance and energy densities. Researchers are examining various transition metal

[a] *School of Physics and Electronic Information, Yunnan Normal University, 768 Juxian Street, Kunming 650500, Yunnan, China.*
E-mail: junaidriaz1990@gmail.com
[b] *Department of Physics, Hazara University, Mansehra 21300, Pakistan.*
E-mail: aminaamni11@gmail.com

oxides (TMOs), including nickel (Ni), cobalt (Co), tin (Sn), manganese (Mn), molybdenum (Mo), and vanadium (V), as electrode materials in supercapacitors to enhance their pseudocapacitive characteristics.[16–20]

Zinc oxide (ZnO) is a crucial and environmentally sustainable semiconductor from the II–VI group, widely applied in diverse technological areas.[21–23] Due to its considerable reactivity in electrochemical applications, ZnO is a crucial component for the active materials of SC electrodes. The ZnO electrode, however, has sluggish faradaic redox kinetics and a limited capacity for high-rate operation, resulting in poor cycling stability. These limitations have been addressed through the exploration of ZnO nanostructures in composite architectures, which improve their electrochemical performance and mitigate these drawbacks.[24,25] Riaz J. constructed a TiN–ZnO composite electrode that demonstrated enhanced supercapacitor performance throughout an extended potential range, attributed to the synergistic interaction between TiN and ZnO and their structured arrangement.[26] Using ZnO nanorods directly deposited on an aluminum substrate, Ahmad *et al.* reported a capacitance value of 394 F g^{-1}, measured at a scan rate of 20 mV s^{-1}.[27] ZnO/graphene nanosheets are reported to have a capacitance of 62.2 F g^{-1} at a current density of 0.5 A g^{-1}.[28] The microwave synthesis of ZnO/graphene nanocomposites has yielded a capacitance of 146 F g^{-1}.[29] The basic properties of SC electrode materials, such as a variety of oxidation states, a long cycle life, affordability, abundance, and non-toxicity, are all fulfilled by iron sulfide (FeS). Extensive efforts have been directed toward synthesizing FeS nanosheets to harness their promising properties. Chodankar *et al.*[30] documented a MnO_2//MnO_2 symmetric supercapacitor exhibiting superior energy storage capabilities within a voltage range of 1.6 V. A supercapacitor device featuring a 1 V potential window was constructed utilizing a nickel cobaltite ($NiCo_2O_4$) nanowire array anchored on a nickel foam electrode.[31]

This study reports the synthesis of FeS sheets and ZnO nanoparticles through a hydrothermal method, followed by the fabrication of an FeS–ZnO composite *via* an efficient wet-chemical process. The FeS–ZnO composite electrode exhibits a notable capacitance (C_s) of 485.10 F g^{-1} at a current density of 1 A g^{-1}. The FeS–ZnO composite exhibits a notable energy density (E_d) of 51.77 Wh kg^{-1} and a power density (P_d) of 4000 W kg^{-1}. The FeS and ZnO particle composite sheets enhance charge mobility by augmenting electrical conductivity and surface area, facilitating electron transfer and ion diffusion. Consequently, the electrode generated by this approach demonstrates considerable potential as a feasible option for deployment in supercapacitor applications (see Table 5 for further comparison).

2. Experimental section

2.1 Materials and methods

The following materials were used in the experiment: ethanol, polyvinylidene fluoride (PVDF), *N*-methyl-2-pyrrolidone (NMP), nickel foam, manganese dioxide (MnO_2), thioacetamide (C_2H_5NS) (99%), zinc chloride ($ZnCl_2$) (98%), acetic acid (AcOH) (99%), and iron(III) chloride hexahydrate ($FeCl_3{\cdot}6H_2O$) (99%). Sinopharm Chemical Reagent Co., Ltd in Beijing provided all of the chemicals, which were of analytical reagent quality. The components were used exactly as they were delivered, requiring no further purification.

Table 1 Composition of FeS–ZnO composite with wt%

Materials	Compositions	FeS	ZnO	Time	Methanol	Temp
FeS–ZnO	FeS–40% ZnO	0.32 g	0.48 g	12 h	40 ml	80 °C

2.2 Synthesis of FeS

FeS sheets were created by dissolving 5.8 g of iron(III) chloride hexahydrate ($FeCl_3{\cdot}6H_2O$) and 6.8 g of thioacetamide (C_2H_5NS) in 15 mL of DI water and 6 mL of ethanol. For 40 minutes, the solution was ultrasonically sonicated to guarantee uniform mixing and improve the nucleation process. To maintain a controlled environment, the resulting solution was then placed in a 50 mL Teflon-lined stainless-steel autoclave. After being sealed, the autoclave was heated to 150 °C for two hours in an oven. FeS sheets with the necessary morphology and crystallinity were made easier by this controlled heating process. To get rid of any residual contaminants or unreacted precursors, the FeS was thoroughly cleaned with ethanol and DI water after the heat treatment. Stable and extremely pure FeS sheets were obtained by vacuum-drying the purified FeS sheets for four hours at 60 °C to eliminate any remaining moisture.

2.3 Synthesis of ZnO

Using the co-precipitation method, ZnO square-shaped NPs were produced by dissolving a stoichiometric amount of $ZnCl_2$ in triple-distilled water, and then gradually adding the resulting solution to an alkaline KOH solution while stirring constantly. The solution was vigorously stirred at 80 °C until the precipitate formed, then repeatedly filtered and washed with ethanol and distilled water. Finally, the precursor was heated for two hours at 100 °C.

2.4 Preparation of FeS–ZnO composite

The FeS–ZnO nanocomposite was created using the FeS and ZnO ratios shown in Table 1. To facilitate the process, 40 mL of methanol was added with continuous agitation to ensure the uniform distribution of the FeS and ZnO. After the materials were thoroughly amalgamated, they underwent sonication. The particles in the fluid were distributed more rapidly due to the adequate agitation of this procedure. Subsequently, the nanocomposite samples were meticulously dried. The samples were dried at a consistent temperature of 80 °C for 12 hours to allow controlled evaporation of the solvent. Once the nanocomposite material solidified, it was ready for investigation, analysis, and potential use as an SC electrode material (Fig. 1).

2.5 Characterization

A Tongda TD-3500 X-ray diffraction (XRD) machine with a Cu K (λ = 1.5403 Å) radiation source was used in this investigation.

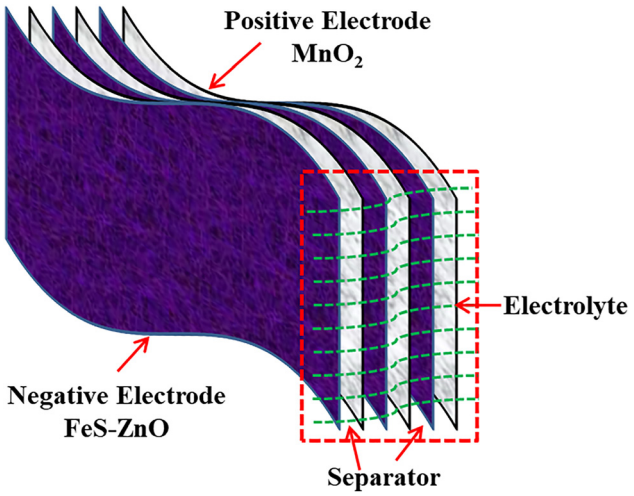

Fig. 1 Schematic representation of FeS–ZnO//MnO_2 supercapacitor.

The produced samples were examined for phase identification, material verification, and crystal structure analysis. A JEOL JSM-7800F instrument was used to do an FESEM examination of the surface. EDX (energy-dispersive X-ray) testing confirmed the elemental analysis. Using an electrochemical workstation (DH7001B), galvanostatic charge/discharge (GCD), cyclic voltammetry (CV), and electrochemical impedance spectroscopy (EIS), the electrochemical characteristics of the nanocomposites were investigated. A 3 M KOH electrolytic solution was used with an Ag/AgCl reference electrode and a platinum foil counter electrode.

2.6 Electrochemical measurements

A slurry was prepared using *N*-methyl-2-pyrrolidone (NMP) as the solvent and polyvinylidene fluoride (PVDF) as the binder, with FeS, ZnO, and FeS–ZnO composite as the active materials supported on conductive carbon. The resulting gel-like paste was uniformly coated onto a small circular nickel-foam carbon sheet. The coated electrodes were then dried at 60 °C for 12 h to obtain the FeS–ZnO composite electrode. After drying, the coated carbon sheet served as the active working electrode. Electrochemical measurements were carried out in a 3E configuration using 3 M KOH as the electrolyte. An Ag/AgCl electrode and a platinum wire were employed as the reference and counter electrodes, respectively, within a potential window of −0.8 to 0.0 V. Cyclic voltammetry (CV), galvanostatic charge–discharge (GCD), and electrochemical impedance spectroscopy (EIS) measurements were performed using the same electrochemical setup. EIS measurements were conducted over a frequency range of 0.1 kHz to 100 kHz within the same potential window. To evaluate the long-term cycling stability, the electrodes were subjected to 10 000 charge–discharge cycles at a current density of 10 A g^{-1}. For the cycling stability tests, platinum foil and Ag/AgCl were used as the counter and reference electrodes, respectively.[32] Each electrode contained

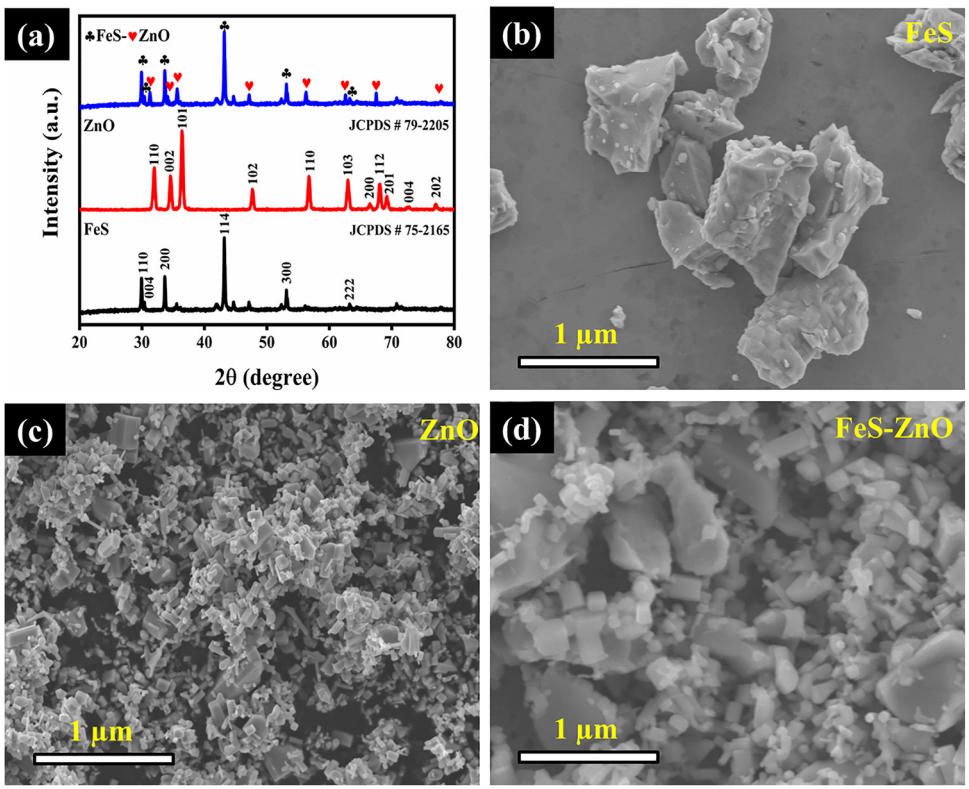

Fig. 2 (a) X-Ray diffraction analysis of FeS, ZnO, and FeS–ZnO, and (b)–(d) field emission scanning electron microscopy of FeS, ZnO, and FeS–ZnO composite.

an active material loading of ~2 mg, ensuring consistent mass normalization for electrochemical measurements.

$$\frac{m+}{m-} = \frac{C-}{C+} \times \frac{V+}{V-} \quad (1)$$

The abovementioned equation illustrates the relationships among the masses, capacitance, and voltages of cathodes and anodes.[33]

2.7 Asymmetric device

The fabrication of asymmetric supercapacitors (ASSC) employs a FeS–ZnO nanohybrid for the negative electrode, MnO_2 for the positive electrode, and an electrospun PVDF membrane infused with 3 M KOH as the separator and electrolyte. The investigation of FeS–ZnO‖MnO_2 based ASSC entailed assessing specific capacitance, power density, and energy density by evaluating the mass of cathode and anode materials using CV and charge/discharge analysis.

$$C_s = \frac{I \times \Delta t}{m \times \Delta V} \quad (2)$$

$$E = \frac{C_s \times \Delta V^2}{7.2} \quad (3)$$

$$P = \frac{3600 \times E}{\Delta t} \quad (4)$$

Where C_s is the electrode's capacitance, Δt is the electrode's discharge time, and ΔV is the voltage difference across the electrode. In the assembled asymmetric supercapacitor (ASC) device, each electrode was prepared with an active material loading of approximately 2 mg, and all electrochemical performance metrics were calculated based on the total active mass of both electrodes.

3. Results & discussion

3.1 Structural analysis

Fig. 2 illustrates the XRD patterns of FeS, ZnO, and the FeS–ZnO nanocomposite, thereby validating their crystalline structures. The diffraction peaks for FeS (JCPDS #75-2165) are observed at 29.9°, 30.4°, 34.7°, 43.2°, 53.1°, and 64.4°, corresponding to the mackinawite FeS crystallographic planes (110), (004), (200), (114), (300), and (222), respectively. Concurrently, the ZnO displays a hexagonal crystal structure with diffraction peaks at 31.7°, 34.4°, 36.1°, 47.6°, 56.6°, 62.8°, 66.4°, 67.9°, 69.1°, 72.6°, and 77.1°, which correspond to the planes (100), (002), (101), (102), (110), (103), (200), (112), (201), (004), and (202) (JCPDS #79-2205). The XRD pattern of the FeS–ZnO nanocomposite exhibits distinct peaks corresponding to both FeS and ZnO, thereby validating the practical synthesis of the nanocomposite and the retention of the crystalline integrity of each constituent. This illustrates the successful incorporation of FeS and ZnO in the produced composite.

$$D = \frac{\kappa\lambda}{\beta \sin\theta} \quad (5)$$

Here, k represents Scherrer's constant, valued at 0.9; the wavelength (λ) is 1.5418 Å; β denotes the full width at half maximum (FWHM) of the diffraction peak; and θ signifies the matching Bragg angle of the crystal plane.

Fig. 2(b)–(d) showcases the surface features of FeS, ZnO, and their composite as captured by FE-SEM analysis. In Fig. 2(b), FeS reveals a loose network of distorted nanosheets with irregular textures. ZnO, depicted in Fig. 2(c), exhibits distinct square-shaped particles with inconsistent surface morphology and a non-uniform size range. When combined, as shown in Fig. 2(d), ZnO nanoparticles are uniformly anchored onto the FeS framework, resulting in a well-integrated hybrid structure. The intertwining of the two components forms a porous matrix with high surface area, allowing enhanced electrolyte interaction and improved ion accessibility. This interconnected architecture is expected to boost charge storage efficiency and support high-performance electrochemical behaviour. Fig. 3 illustrates the elemental compositions of FeS, ZnO, and FeS–ZnO as determined by energy-dispersive X-ray spectroscopy. The EDX spectra of FeS materials show two distinct peaks, three of which correspond to Fe and one to S, as shown in Fig. 3(a). The high-energy region confirmed the peaks at 48.04% and 51.97%, respectively. The EDX spectra of the ZnO nanocomposites showed two distinct peaks in the high-energy region: one at 46.69% for O and another at 53.31% for Zn, indicating the presence of both elements (Fig. 3b). The EDX spectra of FeS–ZnO composites showed four distinct peaks in the high-energy region, which corresponded to O, S, Zn, and Fe, respectively, at 12.97%, 12.66%, 33.54%, and 40.82%. This verifies the existence of O, S, Zn, and Fe, as illustrated in Fig. 3(c). The spectra

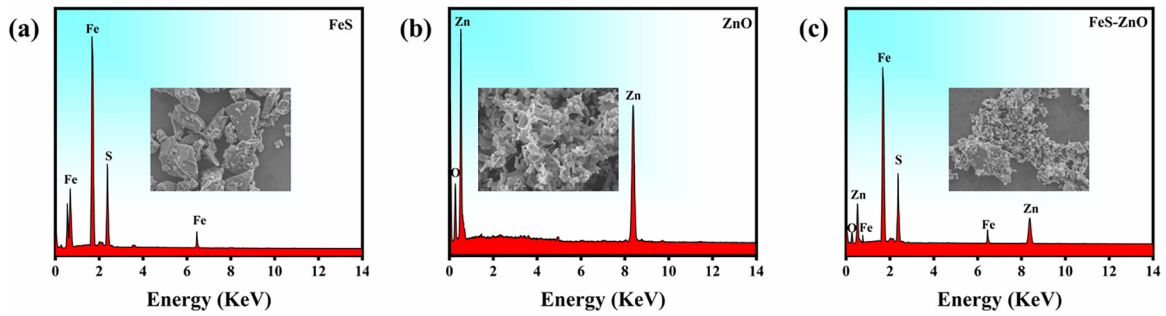

Fig. 3 EDX analysis of (a) FeS, (b) ZnO, and (c) FeS–ZnO composite.

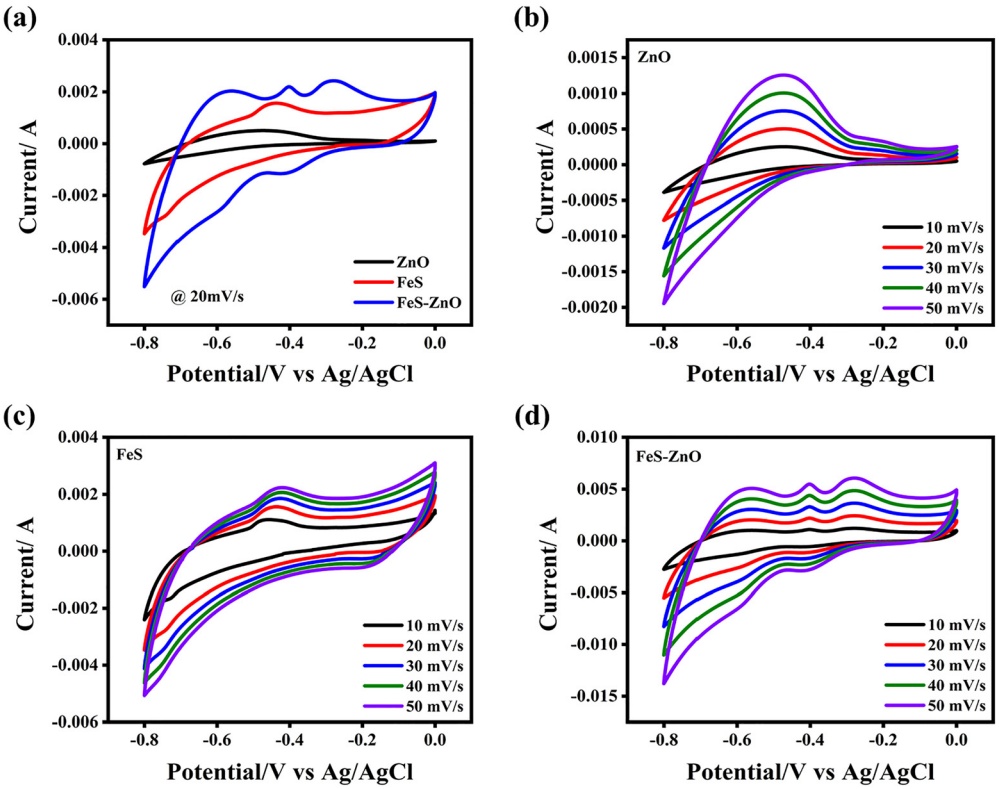

Fig. 4 Cyclic voltammetry of (a) comparison of all electrodes at 20 mV s^{-1}, (b) ZnO, (c) FeS, and (d) FeS–ZnO composite at 10–50 mV s^{-1}.

of the image do not exhibit any additional peaks, confirming the purity of the synthesized FeS–ZnO nanocomposites (Fig. 3c).

4. Electrochemical performance

A three mol L^{-1} KOH electrolyte was used in a three-electrode configuration to study the electrochemical properties of FeS, ZnO, and FeS–ZnO electrodes. Using a scan rate of 20 mV s^{-1} and a potential range of −0.8 to 0.0 V, Fig. 4a shows the CV curves of FeS, ZnO, and FeS–ZnO. Notably, the area of the CV curves at a specified sweep rate and the specific capacitance of the electrode materials are both higher for FeS–ZnO than for FeS and ZnO. This suggests improved capacitance properties for the FeS–ZnO composite electrode material. Here, we describe the oxidation and reduction reactions that take place when electrode materials are submerged in a KOH solution.

$$FeS + 3OH^- \rightarrow Fe(OH)_3 + S + 3e^- \quad (6)$$

$$Fe(OH)_3 + e^- \rightarrow FeS + 3OH^- \quad (7)$$

$$ZnO + 2OH^- + H_2O \rightarrow Zn(OH)_4^{2-} + 2e^- \quad (8)$$

$$Zn(OH)_4^{2-} + 2e^- \rightarrow ZnO + 2OH^- + H_2O \quad (9)$$

Fig. 4(b)–(d) illustrates that during the evaluation of FeS, ZnO, and FeS–ZnO within a scan rate range of 10–50 mV s^{-1}, the area encompassed by the CV curves progressively expanded with the sweep rate. The pseudocapacitive character of the ZnO and FeS electrodes is confirmed by the particular redox peaks visible in their CV curves. This behaviour shows that rapid, reversible faradaic reactions, rather than straightforward electrostatic accumulation, dominate the charge storage mechanism. Rapid charge transfer becomes feasible due to the redox activity resulting from surface or near-surface interactions between the electrode material and the electrolyte. The performance of energy storage is improved, and such pseudocapacitive systems increase capacitance. The increasing regions of the CV curves with scan rate indicate that these electrodes have superior rate capacity and exceptional reversibility. Fig. 4d illustrates the cyclic voltammetry plots for the composite FeS–ZnO, exhibiting quasi-rectangular configurations. The mirror-symmetric CV curves demonstrate excellent electrochemical reversibility and characteristic supercapacitive behavior. The nearly identical response of each device indicates stable operation within the potential window of −0.8 to 0.0 V without noticeable performance degradation.

The capacitive contributions of the ZnO, FeS, and FeS–ZnO composite electrodes were evaluated at scan speeds between 10 and 50 mV s^{-1}, as depicted in Fig. 5. The ZnO electrode (Fig. 5a) demonstrated a capacitive contribution that increased from 17% at 10 mV s^{-1} to 43% at 50 mV s^{-1}, indicating a notable improvement in capacitive behaviour with higher scan rates. The FeS electrode (Fig. 5b) exhibited a capacitive contribution of 23% at 10 mV s^{-1}, which increased to 48% at 50 mV s^{-1}. This improved capacitive response indicates a higher charge storage capacity compared to FeS at both low and high scan rates. The

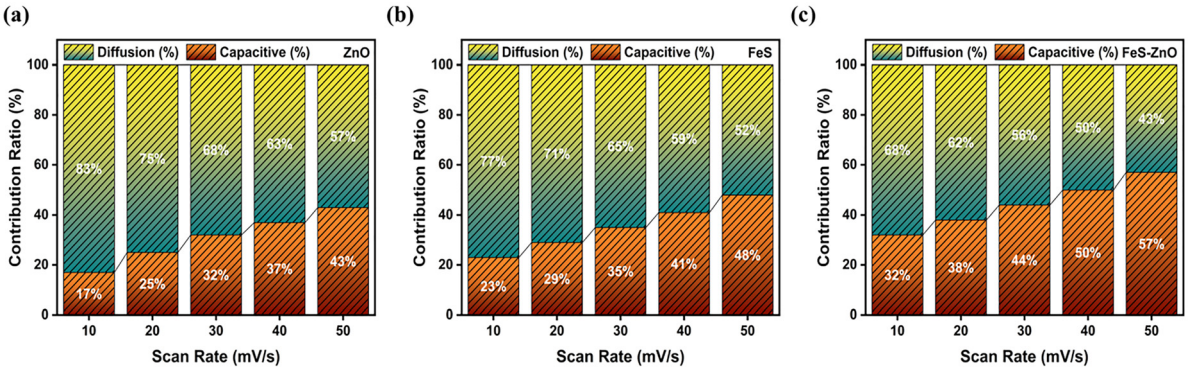

Fig. 5 Capacitive contribution of (a) ZnO, (b) FeS, and (c) FeS–ZnO composite at 10–50 mV s^{-1}.

FeS–ZnO composite (Fig. 5c) outperformed the individual components, demonstrating a capacitive contribution of 32% at 10 mV s^{-1}, significantly increasing to 57% at 50 mV s^{-1}. The interaction between FeS and ZnO in the composite material improves its capacitive performance, suggesting increased ion diffusion and superior charge storage capacities, particularly at high scan rates. The FeS–ZnO composite is a promising material for energy storage applications due to its outstanding capacitive performance across all assessed scan rates.

To gain a more thorough knowledge of the electrochemical reaction kinetics of FeS, ZnO, and FeS–ZnO, we employed an equation to precisely characterize the relationship between peak current and scan rate in the CV curves.

$$i = av^b \tag{10}$$

$$\log i = b \log v + \log a \tag{11}$$

In this context, "i" denotes the peak current, "v" signifies the scan rate, and "a" and "b" are coefficients. In the log(v) log(i) fitting plot, the y-axis intercept denotes parameter a, whereas the slope of the curve signifies parameter b. The kinetics of the process is primarily controlled by diffusion and involves ion intercalation when b ranges from 0 to 0.5. When b lies between 0.5 and 1, it indicates that the Faraday reaction has an impact on the kinetics of response, as it displays significant pseudocapacitive properties. For FeS, ZnO, and FeS–ZnO, the corresponding b values are 0.726, 0.734, and 0.7205. The results suggest that both surface capacitance and diffusion-controlled mechanisms contribute to the charge storage mechanism of the electrode materials. The following formula can be used to calculate the contribution ratio:

$$i(V) = k_1 v + k_2 v^{1/2} \tag{12}$$

$$i/v^{1/2} = k_1 v^{1/2} + k_2 \tag{13}$$

Increasing the scan rate from (10–50) mV s^{-1} Fig. 6a results in a significant increase in the FeS–ZnO ratio, which also rises substantially. The results suggest that diffusion-controlled processes, operating at reduced scan rates, predominantly govern the charge storage mechanism. Nevertheless, as scan rates escalate, the impact of surface capacitance becomes more significant, leading to a reduction in the role of diffusion due to the decreased contact time of the ions with the electrode material. Fig. 6(a) illustrates that the dark blue integration area accounts for roughly 57% of the surface capacitance contribution at a scan rate of 50 mV s^{-1}.

The GCD curves for the FeS, ZnO, and FeS–ZnO electrodes at a current density of 3 A g^{-1} are shown in Fig. 7(a). The specific capacitance of FeS–ZnO (485.10 F g^{-1}) is higher than that of ZnO (172.5 F g^{-1}) and FeS (230 F g^{-1}), as shown by eqn (2). At current densities ranging from 1 to 5 A g^{-1}, the GCD curves of the FeS, ZnO, and FeS–ZnO electrodes are shown in Fig. 7(b)–(d). As the current density rises from 1–5 A g^{-1}, the diffusion and mobility of electrolyte ions on the electrode material's

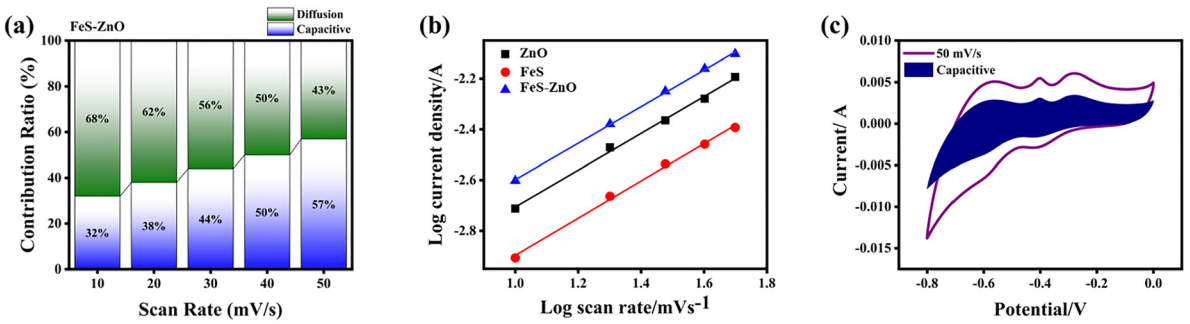

Fig. 6 (a) Contribution ratio of FeS–ZnO composite, (b) b-value of FeS, ZnO, and FeS–ZnO composite, and (c) capacitive performance of FeS–ZnO composite at 50 mV s^{-1}.

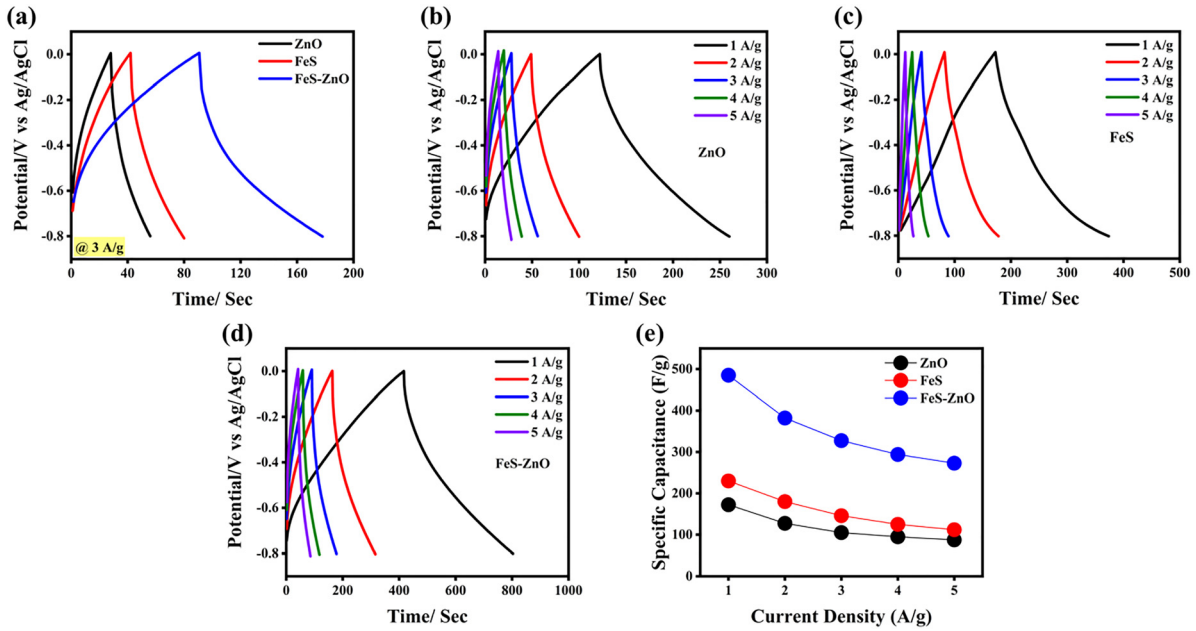

Fig. 7 Galvanostatic charge–discharge performance of (a) all electrode comparison at 3 A g^{-1}, (b) ZnO, (c) FeS, (d) FeS–ZnO composite, and (e) specific capacitance of ZnO, FeS, and FeS–ZnO composite electrode.

surface become more difficult. The limited penetration of charge carriers into the interior of the active material restricts the electrochemical reaction. After that, the specific capacitance value drops. As shown in Fig. 7d, the GCD curves of the FeS–ZnO composite are symmetrical and consistent, aligning well with the CV results and supporting the observed electrochemical behaviour. Fig. 7(b)–(e) illustrates the specific capacitance of the FeS electrode across different current densities. The capacitance values are 230, 180, 146, 125, and 112 F g^{-1} at current densities of 1–5 A g^{-1}. Eqn (2) calculates these values over a voltage range of −0.8 to 0.0 V. The specific capacitances for the ZnO electrode are 172.5, 127.6, 105, 95, and 87.3 F g^{-1}. The specific capacitances of the FeS–ZnO electrode are 485.1, 382.2, 327.6, 294, and 273 F g^{-1}, respectively. As the current density increases from 1 to 5 A g^{-1}, the specific capacitance of FeS decreases from 230 to 112 F g^{-1}, while ZnO shows a similar trend, dropping from 172.5 to 87.3 F g^{-1}. In comparison, the FeS–ZnO composite exhibits a higher initial capacitance of 485.1 F g^{-1}, which decreases to 273 F g^{-1} with increasing current density. Despite this decline, the composite maintains a relatively stable capacity, indicating improved rate capability and synergistic interaction between FeS and ZnO components. Fig. 7(e) illustrates that the composite electrode composed of FeS and ZnO exhibits a greater specific capacitance than electrodes constructed from separate components due to the synergistic interaction between the two materials. The electrochemical performance and capacity are improved by integrating the extensive surface area and conductive pathways of FeS sheets with ZnO nanoparticles, which augment the active sites for charge storage (Table 2).

Table 2 Specific capacitance of all the prepared electrodes

Current density (A g^{-1})	ZnO (F g^{-1})	FeS (F g^{-1})	FeS–ZnO (F g^{-1})
1	172.5	230	485.1
2	127.6	180	382.2
3	105	146	327.6
4	95	125	294
5	87.3	112	273

Fig. 8 presents the electrochemical impedance spectroscopy (EIS) results of the FeS, ZnO, and FeS–ZnO composite electrodes, illustrating both the real (Z') and imaginary (Z'') components of the impedance spectra. In the Nyquist plots, the intercept of the curve with the real axis in the high-frequency region corresponds to the solution resistance (R_s), which reflects the combined resistance of the electrolyte, intrinsic electrode resistance, and contact resistance between the electrode and current collector. The diameter of the semicircular arc observed in the high to medium frequency region represents the charge transfer resistance (R_{ct}), associated with the kinetics of interfacial redox reactions at the electrode–electrolyte interface. In the low frequency region, the nearly vertical line approaching the imaginary axis is indicative of ion diffusion behavior within the electrolyte and electrode material, reflecting ideal capacitive characteristics. All three electrodes FeS, ZnO, and the FeS–ZnO composite exhibit comparable Nyquist plot profiles (Fig. 8a), suggesting similar electrochemical reaction mechanisms. However, quantitative analysis reveals significant differences in resistance parameters. Notably, the FeS–ZnO composite electrode shows substantially lower R_s and R_{ct} values compared with the individual FeS and ZnO electrodes (Fig. 8b), indicating enhanced electrical conductivity and faster charge transfer kinetics. The reduced R_{ct} of the FeS–ZnO composite can be attributed to the effective incorporation of FeS into the ZnO

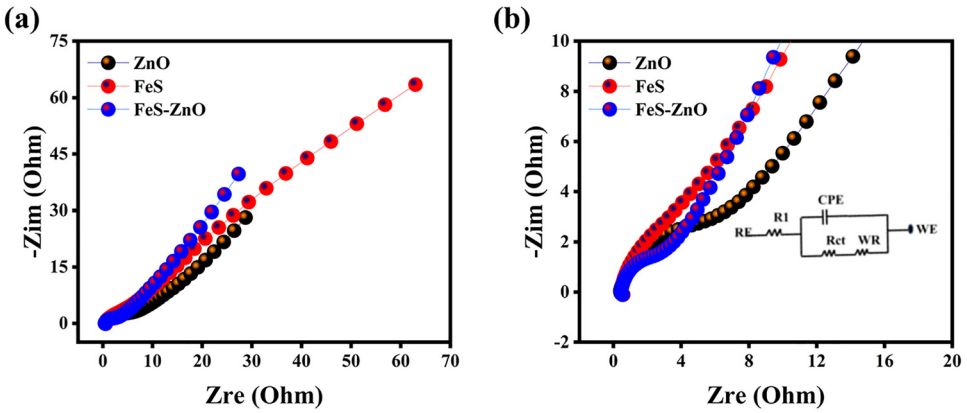

Fig. 8 (a) Impedance plot of FeS, ZnO, and FeS–ZnO composite, (b) zoomed view.

matrix, which facilitates improved electron transport pathways and strengthens interfacial contact within the composite structure. In contrast, the pure ZnO electrode exhibits relatively poor electrical conductivity, leading to higher solution and charge transfer resistances, as evidenced by the increased R_s and R_{ct} values. These elevated resistances result in sluggish interfacial kinetics and inferior electrochemical performance. As summarized in Table 3, the FeS–ZnO composite electrode demonstrates superior electrical conductivity and enhanced capacitive performance relative to the pristine FeS and ZnO electrodes. The synergistic interaction between FeS and ZnO effectively reduces internal resistance, thereby promoting efficient ion diffusion and charge transfer, which ultimately contributes to the improved electrochemical behavior of the composite electrode.

The two-electrode device was engineered to provide sufficient energy storage for practical supercapacitor applications. The enhanced charge storage capacity of the FeS–ZnO nanocomposite electrode was investigated using a two-electrode setup, with 3 M KOH aqueous solutions serving as the electrolyte between the cathode and anode. Fig. 9a illustrates the schematic design of an asymmetric supercapacitor configured with FeS–ZnO as the cathode and MnO_2 as the anode. Fig. 9b presents the working potential ranges of the assembled device, with MnO_2 operating between 0.0 and 0.8 V, and FeS–ZnO between −0.8 and 0.0 V. The ASSC CV curves of FeS–ZnO‖MnO_2 for different scan rates and potentials (−0.8 to 0.8 V) are illustrated in Fig. 8c. The selected voltage is optimal for operation, as the peak voltage reached 1.6 V, according to the CV curves. The voltammogram of the FeS–ZnO‖MnO_2 ASC exhibits a symmetrical pattern at both positive and negative potentials, demonstrating its exceptional reversibility and rate capacity. The overall charge storage capacity in a two-electrode configuration often employed in supercapacitors is associated with the redox peaks detected in FeS–ZnO nanocomposite and MnO_2 aqueous solutions during cyclic voltammetry (CV) analysis. These candidates exhibit potential for energy storage devices owing to the pseudocapacitive characteristics suggested by these peaks. The CD pattern of the FeS–ZnO‖MnO_2 ASSC is represented in Fig. 9d. CD tests were conducted using diverse charge and discharge current rates from −0.8 V to 0.8 V. The capacitance was determined to be 145.62 F g^{-1} at a current of 1 A g^{-1}. The capacitance was maintained at that level by gradually decreasing it until it attained 56 F g^{-1} at a discharge current of 5 A g^{-1}. Fig. 9e illustrates the data for a particular current rate. A unique voltage plateau in the CD platform signifies the behaviour of both EDLCs and pseudo-capacitors within the FeS–ZnO‖MnO_2 ASSC system. The impedance map in Fig. 8f illustrates the best performance of the FeS–ZnO‖MnO_2 ASSC. The FeS–ZnO‖MnO_2 ASSC exhibited elevated conductivity, with an R_s value of 5.054 Ω and an R_{ct} value of 5.417 Ω. Fig. 9f illustrates that the material's elevated conductivity resulted in an enhancement of capacitance.

Power density and energy density are two key parameters for assessing the performance of the FeS–ZnO‖MnO_2 ASSC, and they are calculated using eqn (3) and (4). At a current density of 1 A g^{-1}, we achieved an energy density of 51.77 Wh kg^{-1} and a power output of 800 W kg^{-1}. At a discharge current of 5 A g^{-1}, the values rose to 26.66 Wh kg^{-1} and 4000 W kg^{-1}, respectively (Table 4). This work validates the synergistic interaction of FeS and ZnO inside a composite matrix by assessing adequate energy and power transfer. Evaluating the stability of the FeS–ZnO‖MnO_2 ASC cycle is essential for understanding its value. Fig. 10a illustrates that power densities increase as energy densities decrease. The durability of the FeS–ZnO‖MnO_2 ASSC was evaluated over 10 000 cycles at 10 A g^{-1}, as described in Fig. 10b. The electrochemical process likely entailed continuous structural degradation. Fig. 10b illustrates that the FeS–ZnO‖MnO_2 ASSC retains 96.5% of its initial capacity after 10 000 cycles despite being subjected to a considerably elevated current flow rating.

Table 3 Impedance plot analysis of ZnO, FeS, and FeS–ZnO composite conducted using high-resolution zoom software

Materials	R_s (Ω)	R_{ct} (Ω)
ZnO	0.51	5.78
FeS	0.73	3.26
FeS–ZnO	0.60	2.53

5. Conclusion

This work presents a cost-effective wet-chemical synthesis approach for fabricating FeS–ZnO nanocomposites, designed

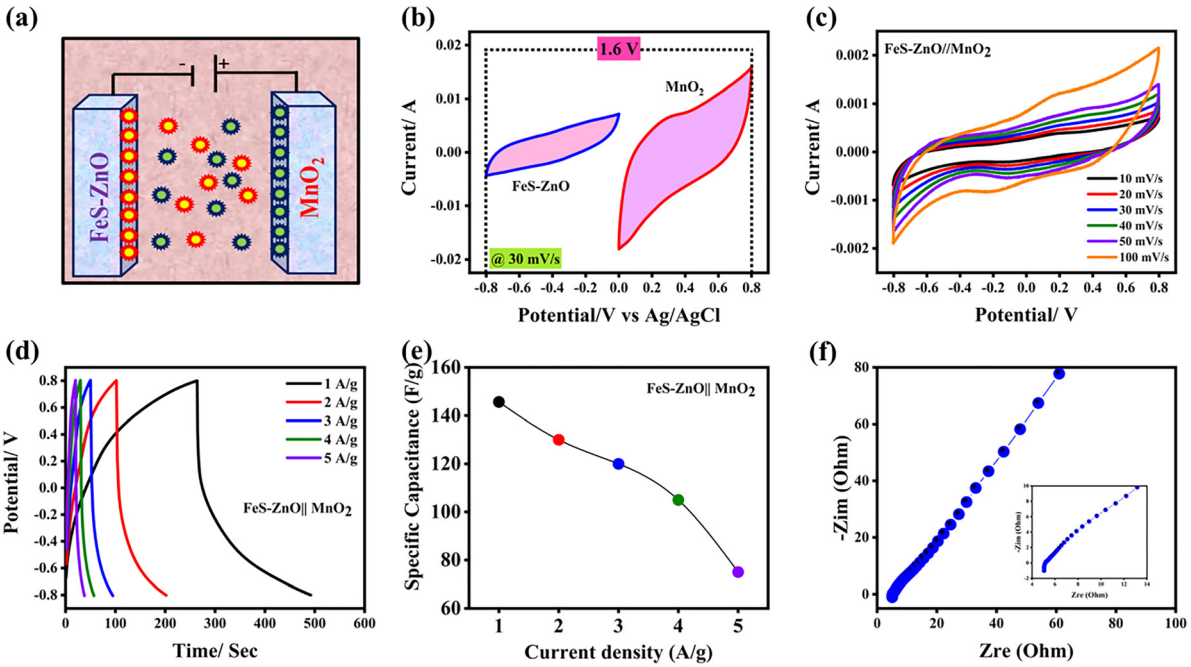

Fig. 9 (a) Schematic representation of an asymmetric supercapacitor FeS–ZnO‖MnO_2, (b) comparative CV of FeS–ZnO and MnO_2 at different potential windows, (c) CV, (d) GCD, (e) specific capacitance, and (f) EIS.

Table 4 FeS–ZnO‖MnO_2 specific capacitance, energy density, and power density at 1–5 A g^{-1}

Current density (A g^{-1})	Specific capacitance (F g^{-1})	Energy density (Wh kg^{-1})	Power density (W kg^{-1})
1	145.62	51.77	800
2	130	46.22	1600
3	120	42.60	2400
4	105	37.32	3200
5	75	26.66	4000

for use as electrode materials in supercapacitor applications. The FeS–ZnO electrode exhibits an impressive specific capacitance of 485.10 F g^{-1} within a potential window of −0.8 to 0.8 V, outperforming both the individual FeS and ZnO electrodes. When assembled into an asymmetric configuration (FeS–ZnO‖MnO_2), with FeS–ZnO as the cathode and MnO_2 as the anode, the device demonstrates excellent rate capability and delivers a specific capacitance of 127 F g^{-1} across a voltage window of 1.6 V. The substantial synergistic effect between the Fe and Zn components is demonstrated by the device's capacity to sustain high conductivity and stability across 10 000 charge–discharge cycles. Additionally, at a peak power output of 3500 W kg^{-1}, it exhibits an exceptional energy density of 45.15 Wh kg^{-1}, demonstrating its potential as a high-performance electrode material for next-generation energy storage applications.

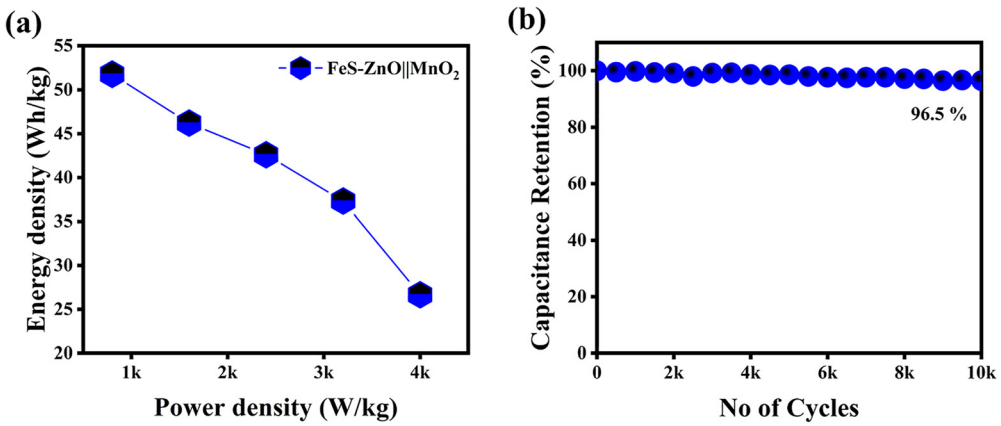

Fig. 10 (a) Energy and power density of FeS–ZnO‖MnO_2, (b) cyclic retention.

Table 5 Comparison of energy density, power density, and cyclic stability of ZnO composite

Materials composite	Energy density (Wh kg^{-1})	Power density (W kg^{-1})	Current density (A g^{-1})	No of cycles	Cyclic retention (%)
Mo@ZnO[34]	39.06	7425	1	8000	75.6
CNO–ZnO@ZnO[35]	10	8100	—	2000	92
ZnO@rGO[36]	50.6	3535	2	2000	96.4
NiO@ZnO[37]	58.3	200	8	6000	82
Nd-doped ZnO[34]	7.36	730	2.5	1000	92
FeS–ZnO [this study]	51.77	4000	10	10 000	96.5

Author contributions

Junaid Riaz: wrote the original manuscript draft, methodology, data curation, characterisation. Amina Bibi: supervision, writing, review, and editing, methodology, software, formal analysis.

Conflicts of interest

The authors declare that they have no conflict of interest.

Data availability

The data that has been used is confidential.

Acknowledgements

This research did not receive any specific grant from funding agencies in the public, commercial, or not-for-profit sectors.

References

1 N. Sisakyan, G. Chilingaryan, A. Manukyan and A. S. Mukasyan, Combustion synthesis of materials for application in supercapacitors: a review, *Nanomaterials*, 2023, **13**(23), 3030.
2 H. Kolavada, P. N. Gajjar and S. K. Gupta, Unraveling quantum capacitance in supercapacitors: Energy storage applications, *J. Energy Storage*, 2024, **81**, 110354.
3 J. Riaz, J. Cao, N. Hakimi, A. Sikandar, F. Aslam, T. Huma and A. Bibi, Synthesis of high-performance supercapacitor electrode materials by wet-chemical route based on TiN–Al 2 O 3 composite, *J. Mater. Sci.: Mater. Electron.*, 2025, **36**(35), 2257.
4 F. Naseri, S. Karimi, E. Farjah and E. Schaltz, Supercapacitor management system: A comprehensive review of modeling, estimation, balancing, and protection techniques, *Renewable Sustainable Energy Rev.*, 2022, **155**, 111913.
5 Y. Huang, M. Gao, Y. Fu, J. Li, F. Wang, S. Yang and R. Wang, Hierarchical porous carbon nanofibers embedded with one-dimensional conjugated metal− organic framework anodes for ammonium-ion hybrid supercapacitors, *Energy Storage Mater.*, 2024, **70**, 103522.
6 J. Riaz, W. Yongyuan, J. Cao, A. Bibi, D. Muhammad, H. Eman and X. Zhou, Wet-Chemical Synthesized TiN–CuO Nanocomposite: Advancing Supercapacitor Technology with High Energy and Power Density, *Phys. E*, 2024, 116105.
7 W. Sugimoto, H. Iwata, Y. Yasunaga, Y. Murakami and Y. Takasu, Preparation of ruthenic acid nanosheets and utilisation of their interlayer surface for electrochemical energy storage, *Angew. Chem., Int. Ed.*, 2003, **42**(34), 4092–4096.
8 J. Riaz, J. Cao, A. Bibi, M. Arif and D. Muhammad, Hydrothermal synthesis of ball-like ZnS nanospheres decorated urchin-like W18O49 nanospheres as electrode for high power and stable hybrid supercapacitor, *Mater. Lett.*, 2024, **370**, 136853.
9 Q. Z. Zhang, D. Zhang, Z. C. Miao, X. L. Zhang and S. L. Chou, Research progress in MnO2–carbon based supercapacitor electrode materials, *Small*, 2018, **14**(24), 1702883.
10 D. Modupeola and P. Popoola, High entropy nanomaterials for energy storage and catalysis applications, *Front. Energy Res.*, 2023, **11**, 1149446.
11 S. Jia, Q. Zhao, M. He and T. Zhang, Hierarchical construction of amorphous NiCo-OHS@ ZnS hollow spheres with optimized reaction kinetics *via* ion exchange-etching strategy for energy storage, *Chem. Eng. J.*, 2024, **494**, 153215.
12 J. Riaz, Y. Zhang, J. Cao, A. Bibi, Z. Zhang and X. Zhou, High-performance electrode material synthesis via wet-chemical method: a study on NbN–Fe2O3 composite, *J. Mater. Sci.: Mater. Electron.*, 2024, **35**(17), 1176.
13 Z. J. Han, S. Pineda, A. T. Murdock, D. H. Seo, K. K. Ostrikov and A. Bendavid, RuO 2-coated vertical graphene hybrid electrodes for high-performance solid-state supercapacitors, *J. Mater. Chem. A*, 2017, **5**(33), 17293–17301.
14 X. W. Wang, D. L. Zheng, P. Z. Yang, X. E. Wang, Q. Q. Zhu, P. F. Ma and L. Y. Sun, Preparation and electrochemical properties of NiO-Co3O4 composite as electrode materials for supercapacitors, *Chem. Phys. Lett.*, 2017, **667**, 260–266.
15 M. Zhang, H. Zheng, H. Zhu, Z. Xu, R. Liu, J. Chen and H. Cui, Graphene-wrapped MnO2 achieved by ultrasonic-assisted synthesis applicable for hybrid high-energy supercapacitors, *Vacuum*, 2020, **176**, 109315.
16 C. Yuan, L. Yang, L. Hou, L. Shen, X. Zhang and X. W. D. Lou, Growth of ultrathin mesoporous Co 3 O 4 nanosheet arrays on Ni foam for high-performance electrochemical capacitors, *Energy Environ. Sci.*, 2012, **5**(7), 7883–7887.
17 X. Zhang, P. Yu, H. Zhang, D. Zhang, X. Sun and Y. Ma, Rapid hydrothermal synthesis of hierarchical nanostructures assembled from ultrathin birnessite-type MnO2 nanosheets for supercapacitor applications, *Electrochim. Acta*, 2013, **89**, 523–529.
18 J. Riaz, F. Aslam, M. Arif, T. Huma and A. Bibi, First investigation of high-performance FeS-based W 18 O 49 asymmetric supercapacitors operating at 1.6 V, *Nanoscale Adv.*, 2025, **7**(1), 231–241.
19 R. B. Pujari, V. C. Lokhande, V. S. Kumbhar, N. R. Chodankar and C. D. Lokhande, Hexagonal microrods architectured MoO 3 thin film for supercapacitor application, *J. Mater. Sci.: Mater. Electron.*, 2016, **27**, 3312–3317.
20 N. Hassan, J. Riaz, M. T. Qureshi, A. Razaq, M. Rahim, A. M. Toufiq and A. Shakoor, Vanadium oxide (V 2 O 3) for energy storage applications through hydrothermal route, *J. Mater. Sci.: Mater. Electron.*, 2018, **29**, 16021–16026.

21 L. S. R. Rocha, C. R. Foschini, C. C. Silva, E. Longo and A. Z. Simões, Novel ozone gas sensor based on ZnO nanostructures grown by the microwave-assisted hydrothermal route, *Ceram. Int.*, 2016, **42**(3), 4539–4545.
22 P. S. Khare, R. Yadav and A. Swarup, RGO-ZnO nanocomposit material of enhanced absorbance for solar energy conversion, *Int. J. Appl. Phys. Math.*, 2013, **3**(2), 95.
23 L. Zhang, L. Du, X. Cai, X. Yu, D. Zhang, L. Liang and J. Song, Role of graphene in great enhancement of photocatalytic activity of ZnO nanoparticle–graphene hybrids, *Phys. E*, 2013, **47**, 279–284.
24 F. Naeem, S. Naeem, Z. Zhao, G. Q. Shu, J. Zhang, Y. Mei and G. Huang, Atomic layer deposition synthesized ZnO nanomembranes: a facile route towards stable supercapacitor electrode for high capacitance, *J. Power Sources*, 2020, **451**, 227740.
25 C. H. Kim and B. H. Kim, Zinc oxide/activated carbon nanofiber composites for high-performance supercapacitor electrodes, *J. Power Sources*, 2015, **274**, 512–520.
26 J. Riaz, J. Cao, Y. Zhang, A. Bibi and X. Zhou, Facile synthesis and electrochemical analysis of TiN-based ZnO nanoparticles as promising cathode materials for asymmetric supercapacitors, *Nanoscale Adv.*, 2024, **6**(20), 5145–5157.
27 T. Ahmad, B. M. Alotaibi, A. W. Alrowaily, H. A. Alyousef, A. Dahshan, A. M. A. Henaish and K. Ahmad, Development of ZnO/AlFeO3 composite via hydrothermal method as supercapacitor electrode, *J. Sol-Gel Sci. Technol.*, 2024, 1–15.
28 J. Wang, Z. Gao, Z. Li, B. Wang, Y. Yan, Q. Liu and Z. Jiang, Green synthesis of graphene nanosheets/ZnO composites and electrochemical properties, *J. Solid State Chem.*, 2011, **184**(6), 1421–1427.
29 T. Lu, L. Pan, H. Li, G. Zhu, T. Lv, X. Liu and D. H. Chua, Microwave-assisted synthesis of graphene–ZnO nanocomposite for electrochemical supercapacitors, *J. Alloys Compd.*, 2011, **509**(18), 5488–5492.
30 N. R. Chodankar, D. P. Dubal, G. S. Gund and C. D. Lokhande, A symmetric MnO2/MnO2 flexible solid state supercapacitor operating at 1.6 V with aqueous gel electrolyte, *J. Energy Chem.*, 2016, **25**(3), 463–471.
31 M. Arif, J. Riaz, A. Bibi, H. Yang and T. Zhu, Enhancing supercapacitor energy density by TiN–ZnS composites unveiled as a promising electrode, *APL Mater.*, 2024, **12**, 071119.
32 J. Riaz, Y. Zhang, J. Cao, A. Bibi, M. Arif, Z. Zhang and X. Zhou, Facile synthesis of TiN nano sheets decorated Fe2O3 nanoparticles as novel cathode material for Asymmetric Supercapacitor, *Surf. Interfaces*, 2024, **46**, 104080.
33 J. Riaz, J. Cao, Y. Zhang, A. Bibi, M. Arif, Z. Zhang and X. Zhou, Improved performance of TiN nano buds decorated MoS2 sheets in asymmetric supercapacitors, *J. Mater. Sci.: Mater. Electron.*, 2024, **35**(17), 1142.
34 A. Ali, M. Ammar, M. Ali, Z. Yahya, M. Y. Javaid, S. ul Hassan and T. Ahmed, Mo-doped ZnO nanoflakes on Ni-foam for asymmetric supercapacitor applications, *RSC Adv.*, 2019, **9**(47), 27432–27438.
35 D. Mohapatra, S. Parida, S. Badrayyana and B. K. Singh, High performance flexible asymmetric CNO-ZnO//ZnO supercapacitor with an operating voltage of 1.8 V in aqueous medium, *Appl. Mater. Today*, 2017, **7**, 212–221.
36 A. Dutta, S. Mishra, S. K. Saha, S. Sarkar, A. Guchhait and A. J. Akhtar, Boosting the supercapacitive performance of ZnO by 3-dimensional conductive wrapping with graphene sheet, *J. Inorg. Organomet. Polym. Mater.*, 2022, **32**(1), 180–190.
37 R. Ahmad, M. Yousuf, A. Mir and M. A. Shah, A Facile One-Step Hydrothermal Synthesis of a Novel Nio/Zno Nanorod Composite for Supercapacitor Application. *Zno Nanorod Composite for Supercapacitor Application*.